iScience

CellPress
OPEN ACCESS

Article

# High-sensitivity, ultrawide linear range, antibacterial textile pressure sensor based on chitosan/MXene hierarchical architecture

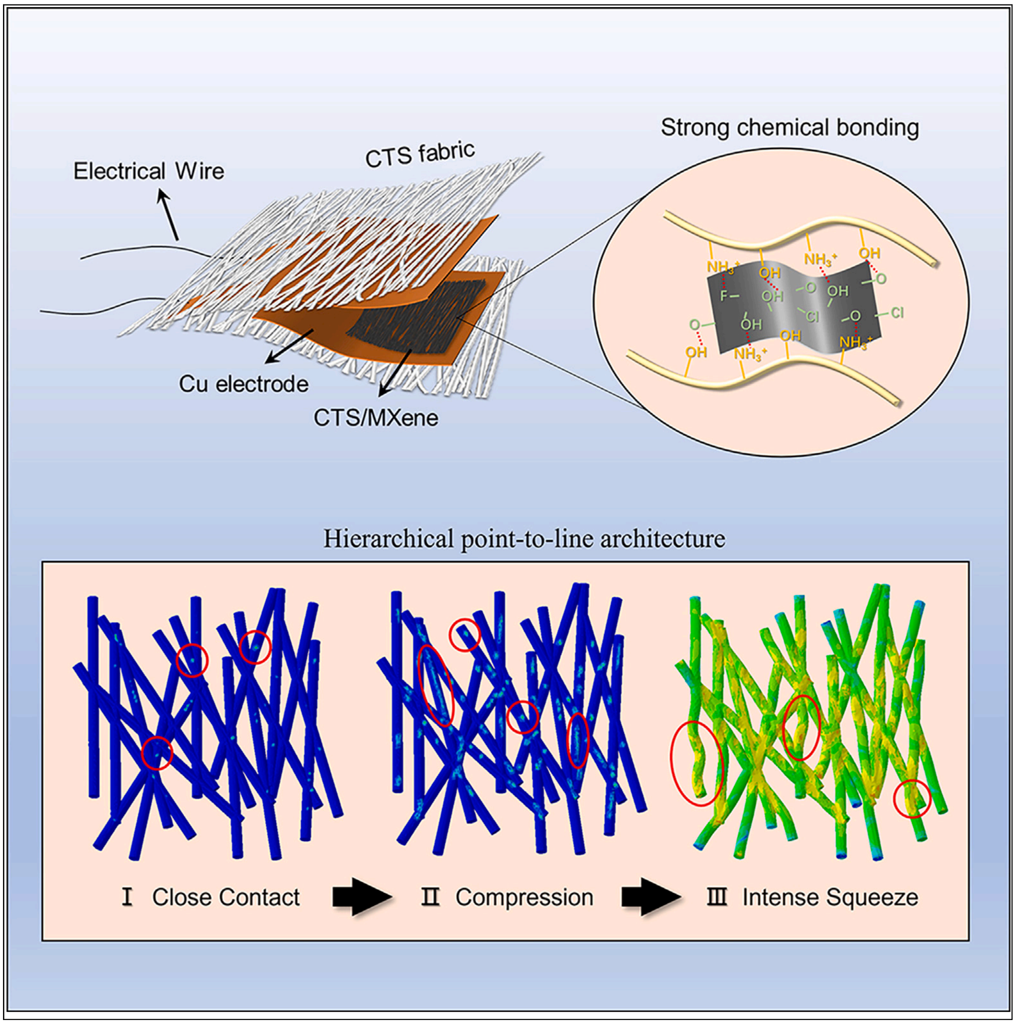

Mengxi Gu, Xuan Zhou, Jienan Shen, ..., Lei Wei, Chunlei Yang, Ming Chen

gq.gu@siat.ac.cn (G.G.)
lei.wang1@siat.ac.cn (L.W.)
wei.lei@ntu.edu.sg (L.W.)
cl.yang@siat.ac.cn (C.Y.)
ming.chen2@siat.ac.cn (M.C.)

## Highlights

A 'point-to-line' architecture and a strong chemical bonding strategy is developed

The sensor exhibits high sensitivity and ultra-broad linearity range

An overall classification rate of 98.61% on six human actions is achieved

The high-performance pressure sensor shows the merit of antibacterial

Gu et al., iScience 27, 109481
April 19, 2024 © 2024 The Authors. Published by Elsevier Inc.
https://doi.org/10.1016/j.isci.2024.109481

iScience

CellPress
OPEN ACCESS

Article

# High-sensitivity, ultrawide linear range, antibacterial textile pressure sensor based on chitosan/MXene hierarchical architecture

Mengxi Gu,[1,2,5] Xuan Zhou,[1,3,5] Jienan Shen,[1] Ruibin Xie,[1] Yuhan Su,[1,2] Junxue Gao,[1,3] Binzhe Zhao,[1,2] Jie Li,[1,2] Yingjie Duan,[1,3] Zhixun Wang,[4] Yougen Hu,[1] Guoqiang Gu,[1,*] Lei Wang,[1,*] Lei Wei,[4,*] Chunlei Yang,[1,2,*] and Ming Chen[1,2,6,*]

## SUMMARY

**It is still a great challenge for the flexible piezoresistive pressure sensors to simultaneously achieve wide linearity and high sensitivity. Herein, we propose a high-performance textile pressure sensor based on chitosan (CTS)/MXene fiber. The hierarchical "point to line" architecture enables the pressure sensor with high sensitivity of 1.16 kPa$^{-1}$ over an ultrawide linear range of 1.5 MPa. Furthermore, the CTS/MXene pressure sensor possesses a low fatigue over 1000 loading/unloading cycles under 1.5 MPa pressure load, attributed to the strong chemical bonding between CTS fiber and MXene and excellent mechanical stability. Besides, the proposed sensor shows good antibacterial effect benefiting from the strong interaction between polycationic structure of CTS/MXene and the predominantly anionic components of bacteria surface. The sensor is also applied to detect real-time human action, an overall classification accuracy of 98.61% based on deep neural network-convolutional neural network (CNN) for six human actions is realized.**

## INTRODUCTION

The extensive developments of flexible pressure sensors have engaged new application opportunities for robotics,[1] human-machine interface,[2] and health monitoring.[3,4] The working mechanism of the pressure sensors can be divided into piezoresistive,[5–8] piezoelectric,[9] capacitive,[10–12] ferroelectric,[13] and triboelectric.[14] Among these pressure sensors, piezoresistive pressure sensors have been widely adopted because of their simple device structure and easy signal processing. The practical applications of piezoresistive pressure sensors lie on their sensing performance especially high sensitivity over a wide linearity for easy signal processing,[15] which is mainly depending on the deformation behavior of elastomers (such as polydimethylsiloxane (PDMS),[16] polyurethane (PU),[17,18] polyimide (PI),[19,20] etc.) as well as active materials (such as metal wires,[21] MXene,[22] carbon nanotubes (CNT),[23] graphene,[24] etc.).

To date, many approaches have been developed to improve these attributes. A classic way to achieve high sensitivity and linearity is to engineer these elastomers with specific patterned micro/nanostructures or random microstructures templated from natural/existing objects (such as leaf,[25,26] abrasive paper,[27] or animal organ[28]). For example, a highly sensitive bionic PDMS/CNT based piezoresistive pressure sensor was rationally designed and realized by employing the Epipremnum aureum leaf and sugar (83.9 kPa$^{-1}$ within 140 Pa).[29] Li et al. achieved high sensitivity piezoresistive pressure sensor by adopting the conical frustum-like PDMS/Ag microstructure (259.32 kPa$^{-1}$ in the range of 0–2.5 kPa)[30] and the spontaneously formed flower-shaped $SnSe_2$ nanoplates (433.22 kPa$^{-1}$ in the range of 0–2.4 kPa).[31] However, the high sensitivity drastically decreases as the pressure further increases. The fabrication of these micro/nanostructured elastic polymers usually requires complex and high-cost production processes, such as UV lithography (photoresist coating, exposure, acid etching, stripping, and so on), inductively coupled plasma (ICP) etching, etc. Several advanced microstructures fabrication methods have been proposed, such as laser etching,[32] which is non-toxic and fast. To prepare deformable sensors or functional circuits on 3D freeform surfaces, Yang et al.[33] developed a well-performed iontronic pressure sensor by laser-induced gradient micro-pyramids. Moreover, decoupling sensing mechanisms is crucial for multimodal sensors, methods like employing force-dependent contact spots between conductive materials and electrodes is an effective way to analyze different signals of compression, bending, and twisting.[34,35] Supplementary work like standalone wearable devices designing is important for practical applications, especially multifunctional platform which is wireless, portable, and multimodal.[36–38]

---

[1] Shenzhen Institute of Advanced Technology, Chinese Academy of Sciences, Shenzhen 518055, People's Republic of China
[2] University of Chinese Academy of Sciences, Beijing 100049, People's Republic of China
[3] Department of Nano Science and Technology Institute, University of Science and Technology of China, Suzhou 215123, People's Republic of China
[4] School of Electrical and Electronic Engineering, Nanyang Technological University, 50 Nanyang Avenue, Singapore 639798, Singapore
[5] These authors contributed equally
[6] Lead contact
*Correspondence: gq.gu@siat.ac.cn (G.G.), lei.wang1@siat.ac.cn (L.W.), wei.lei@ntu.edu.sg (L.W.), cl.yang@siat.ac.cn (C.Y.), ming.chen2@siat.ac.cn (M.C.)
https://doi.org/10.1016/j.isci.2024.109481

iScience 27, 109481, April 19, 2024

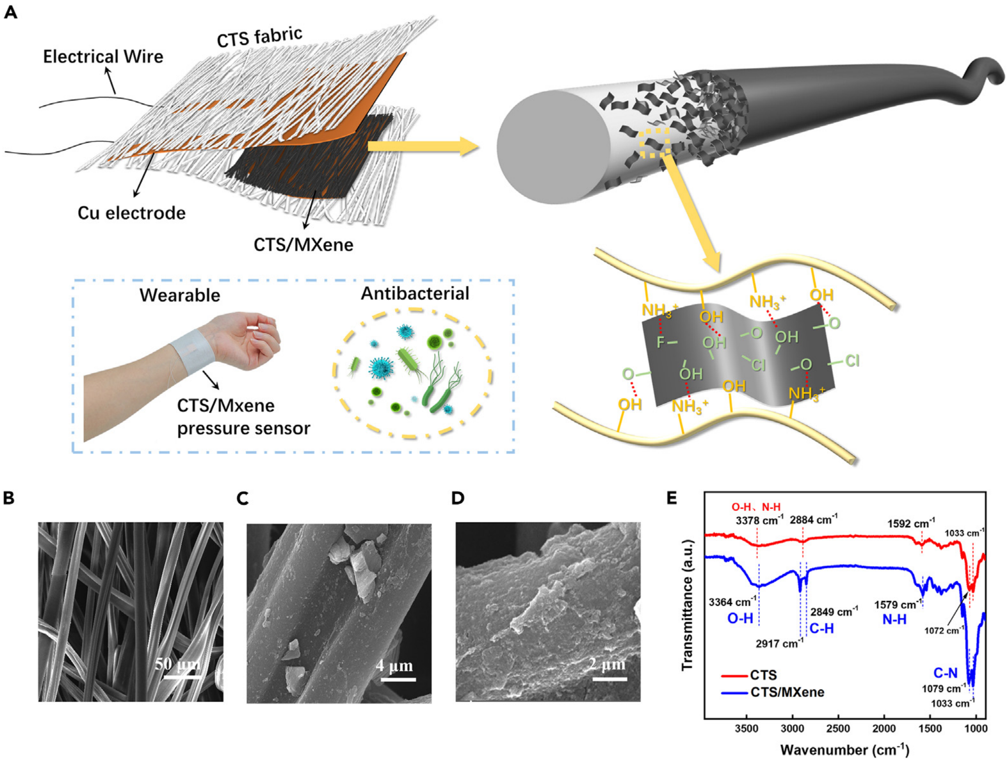

**Figure 1. Fabrication process, application, and characterization of the CTS/MXene pressure sensor and CTS/MXene fabrics**

(A) Structure elaboration, chemical principle and application of the CTS/MXene pressure sensor.

(B–D) Top-view SEM images of CTS, CTS/MXene (stirring) and CTS/MXene (EPD).

(E) FT-IR spectra of CTS and CTS/MXene (EPD).

Besides the requirement of micro/nanostructures, elastic modulus of the sensing material (both the elastomers and active materials) is also the key influence factor of the wide linearity. Conventional PDMS elastomers are commonly subject to the deficiency of low elastic modulus (10 kPa–10 MPa),[39] which may result in the saturation behavior of the pressure sensor at low-pressure levels. High elastic modulus elastomers, such as PI[40] and chitosan (CTS)[41,42] (elastic modulus ~ GPa), are appropriate choice to achieve wide linearity. For instance, Jia et al.[20] reported a PI/FCNT (functional carbon nanotubes) pressure sensor with high-linearity (3380 kPa) via the point-to-point working mechanism, however, at a cost of reduced sensitivity (0.005 $kPa^{-1}$). Therefore, it is still a great challenge for the flexible piezoresistive pressure sensors to simultaneously achieve wide linearity and high sensitivity.

Herein, we demonstrate a thin (~0.76 mm), lightweight (~0.182 $g/cm^3$), wearable, and antibacterial textile CTS/MXene fiber pressure sensor with high sensitivity and ultrawide linear range (Figure 1A). CTS is a natural linear polysaccharide comprised N-acetyl-D-glucosamine and β-(1–4)-linked D-glucosamine, which can be extracted by the alkaline deacetylation of chitin.[43,44] CTS has numerous features such as antibacterial, biodegradability, cationic nature, non-allergic, and non-toxicity.[45] MXenes are a new type of two-dimensional (2D) transition metal carbides formulated as $M_{n+1}X_nT_x$, where M is an early transition metal, X is C and/or N, T is a surface termination O, OH, F, and/or Cl, n is 1–3.[46,47] MXene possesses various merits such as high conductive, hydrophilic, and strong mechanical properties,[48] which have also been proven to be a good candidate for active materials attributing to their excellent diversified structure and controllable electrical properties. The designed CTS/MXene pressure sensor achieves high sensitivity (1.16 $kPa^{-1}$), ultrawide linear range (1.5 MPa, $R^2 = 0.997$), low fatigue over 1000 loading/unloading cycles and small hysteresis of 5.14% even under a high pressure of 1.5 MPa. This is attributed to the synergistic effect of continuous yet large variations of contacting area enabled by the hierarchical "point to line" architecture, strong chemical bonding interaction between CTS and MXene and excellent mechanical stability (Figure 1A). The proposed CTS/MXene pressure sensor also displays good antibacterial effect benefiting from the strong interaction between polycationic structure of CTS/MXene and the predominantly anionic components of bacteria surface. Furthermore, the sensor is applied to recognize human action, an overall classification accuracy of 98.61% for six human actions is realized through a deep neural network based on convolutional neural network (CNN).

## RESULTS AND DISCUSSION

For fabric flexible pressure sensor, a uniform and conductive structure is essential. CTS fabric provides a stable hierarchical network structure which ensures the adsorption of conductive active substances. MXene is a beneficial conductive nanomaterial, which also has excellent mechanical properties. The compression of CTS fabrics wrapped with MXene nanoplates causes gradually increasing contact area, result in resistance reduction. Figure S1 shows the optical micrographs and 3D stereoscopic topography of the CTS fabric. Figure 1B represents the corresponding scanning electron microscope (SEM) image. Hierarchical, porous fiber network with certain orientation is observed, providing both the point-to-point and line-to-line contacting modes under pressure. Compared with the conventional point-to-point contacting mode, these diversified modes may be beneficial to enhance the sensitivity and sensing range. Electrophoretic deposition (EPD) process was employed to construct the CTS/MXene fiber composites (see STAR methods). A uniform and conductive CTS/MXene composite was obtained and the degree of uniformity is much better than that of the frequently used stirring process (MXene tends to agglomerate and gather at the surface or the gap of the fiber network), as observed in Figures 1B–1D. Fourier transform infrared spectroscopy (FT-IR) spectra are adopted to probe the interactions between CTS and MXene (Figure 1E). Several characteristic adsorption peaks of CTS were noted at 3378 $cm^{-1}$, 2884 $cm^{-1}$, and 1592 $cm^{-1}$, corresponding to the stretching vibrations of O–H and N–H, C−H, and N−H, respectively. The bands centered at 1072 $cm^{-1}$ and 1033 $cm^{-1}$ are due to C−N stretching vibration. For CTS/MXene, the broadband at 3378 $cm^{-1}$ shifted to 3364 $cm^{-1}$ and the intensity is significantly reduced, which reveals that hydrogen bonding forms among the surface functional groups such as −OH, =O and $-NH_3^+$ within CTS and MXene (Figure 1A).[49,50] Moreover, in the range of 2950–2800 $cm^{-1}$, new peaks appeared at 2917 $cm^{-1}$ and 2849 $cm^{-1}$, which can be attributed to symmetric and asymmetric stretching vibrations of C−H bonds on MXene functionalized surfaces.[51–54] Besides, the absorption band of N−H shifted to 1579 $cm^{-1}$ and the C−N stretch vibration absorption band shifted to 1079 $cm^{-1}$. This could be also ascribed to the strong chemical interaction between CTS and MXene, originated from the surface functional groups (−OH, =O, −F, −Cl) of delaminated MXene nanoplates ($Ti_3C_2T_x$) through the etching of MAX ($Ti_3AlC_2$) precursors in LiF/HCl mixing solution and ultrasonic-assisted treatment, as well as abundant active surface groups of CTS (−OH, $-NH_2$).

To evaluate the property of the CTS/MXene pressure sensor, we set up an intelligent testing and data-acquisition platform to perform pressure loading and record the corresponding current signal (see STAR methods). The effects of the MXene morphology and doping technique, as well as EPD time on the sensitivity and linearity of the proposed CTS/MXene pressure sensors were systematically studied. Figure S2 is the optical image of the final encapsulated sensor device. The size of the sensor device is 35 mm (length)×35 mm (width)×0.76 mm (thickness) for all the encapsulated CTS/MXene pressure sensors (see STAR methods). Figure 2A shows the relative change of the current ($\Delta I/I_0$) as the pressure load changes, where $\Delta I = I - I_0$, I is current at load pressure, $I_0$ is the initial current. The sensitivity is defined by the following equations: $S=(\Delta I/I_0)/\Delta P$, where ΔP is the pressure change. It is clear that all the CTS/MXene pressure sensors with EPD process exhibit higher sensitivity and broader sensing range than that with stirring process. Furthermore, we can see that EPD time plays critical roles on both the sensitivity and linearity of the CTS/MXene (EPD) sensor device. First of all, the CTS/MXene (EPD) with 1 h EPD time possesses the highest performance with the sensitivity of 1.16 $kPa^{-1}$ over a whole ultrawide linear range of 1.5 MPa. The initial current is quite small (~0.9 μA), making the device sensitive enough. When subjected to a pressure of 1.5 MPa, the current reaches 1.57 mA. Sample-to-sample variations of pressure sensitivity have shown in Figure S3, revealing good uniformity between different CTS/MXene-3 (EPD-1h) pressure sensors. The maximum sensing pressure of CTS/MXene pressure sensor is 3 MPa, as shown in Figure S4. The best linear range is 0–1.5 MPa, and from 1.65 MPa, the current change rate tends to saturate. In the low-pressure region, our pressure sensor can reach a limit of detection as low as 5.14 Pa with a piece of PEEK film (Figure S5). The CTS/MXene (EPD) pressure sensor (EPD time = 0.5 h) shows a relative low sensitivity (0.53 $kPa^{-1}$). This is mainly due to that the CTS fibers are only partially coated by the MXene nanoplates, in other words, the effectively established conductive path is not enough (Figure S6). As the EPD process time increases to 1.5 h, the CTS/MXene (EPD) sensor shows the lowest sensitivity (0.41 $kPa^{-1}$), which can be ascribed to the relatively high initial current (low initial resistance) and fewer conductive paths increasing. Under the electric field, the excess MXene nanoplates not only wrap around CTS fibers, but also fill the fiber gaps due to the stacking via van der Waals forces.[46,55,56] As shown in Figure S6, when EPD time = 1.5 h, MXene nanoplates fill most of the fiber voids and gaps between fiber layers, which greatly reduced the initial resistance of the whole device. The initial resistance is about 526 kΩ ($R_0$ = 1 V/1.9 μA = 526 kΩ). Under the external pressure of 1.5 MPa, the current could reach ~1.17 mA. However, the current change ($\Delta I/I_0$) is not at par with to that of CTS/MXene (EPD) sensor with 1 h EPD process. Table S1 organizes and discusses the effects of four CTS preparation methods on initial conductivity, as well as the corresponding morphology images of the obtained CTS/MXene functional layers. Figure 2B shows the $\Delta I/I_0$ versus pressure curves under loading and unloading in the whole 1.5 MPa working pressure region. The hysteresis of the CTS/MXene (EPD) pressure sensor is estimated to be 5.14%, which is calculated by the formula $\xi_H = \frac{\Delta H_{max}}{Y_{F.S.}}$, where $\Delta H_{max}$ is the maximum difference of the current output between forward and reverse strokes, $Y_{F.S.}$ is the full-scale output current value, as shown in Figure S7. The value is relatively small compared to previous reported piezoresistive pressure sensor. This is because the porous nature of the CTS/MXene architecture that minimizes viscoelasticity as well as its relatively large elastic modulus. To further verify the operational stability and reproducibility of the proposed CTS/MXene (EPD) pressure sensor, different pressures ranging from 80 kPa to 1.5 MPa over 7 on/off cycles were applied to the sensor, as shown in Figure 2C. It is obvious that the CTS/MXene (EPD) sensor responds to the pressure repeatedly with stable current signals under each external pressure, revealing that the proposed sensor could work steadily from kPa to MPa range. The robust repeatability and reliability of the proposed sensor was further confirmed by the repeated high pressure (1.5 MPa) loading and unloading experiments (Figure 2D). Inset of Figure 2D shows the magnified sensor responses at different time intervals. During 1000 repeated cycles, it is observed that there is no obvious signal degradation, attributing to the strong chemical interaction between CTS and MXene as well as outstanding compressibility for CTS and CTS/MXene composites. For mechanical deformation, the proposed CTS/MXene (EPD) pressure sensor device also exhibits excellent repeatability during cyclic bending test and twisting test, as depicted in Figure S8. To further explore the underlying mechanism of the good robustness of the pressure sensor, CTS fiber and CTS/MXene fiber composites were subjected to cyclic compression tests. The results are shown in Figure S9. It is found that both CTS and CTS/MXene exhibits a small plastic strain of 1.5% and 0.5% after 100 cycles at the stress of 1.33 MPa, indicating the outstanding cyclic compressive stability. Figure S10 is the current−voltage (I−V) curves of the sensor

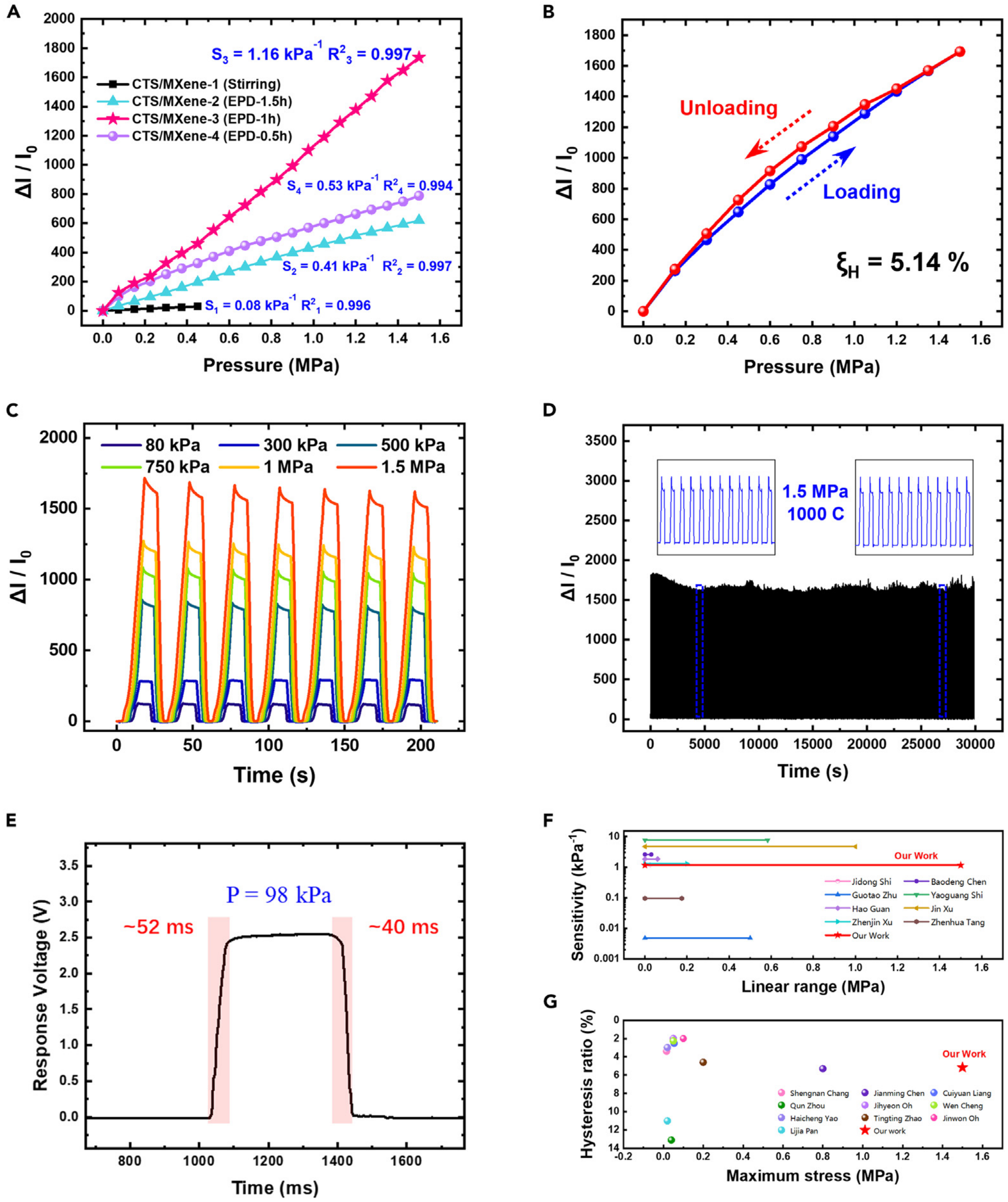

**Figure 2. Pressure sensing performance of the fabricated CTS/MXene pressure sensors**

(A) Relative current change ($\Delta I/I_0$) versus the pressure of the CTS/MXene (stirring), CTS/MXene (EPD-1.5h), CTS/MXene (EPD-1h), CTS/MXene (EPD-0.5h) pressure sensor.

(B) Electrical hysteresis of the CTS/MXene pressure sensor obtained during loading and unloading process in the range of 0–1.5 MPa.

(C) Multiple cycles of the pressure sensor response under different pressures ranging from 80 kPa to 1.5 MPa.

(D) Test of durability of 1000 cycles under 1.5 MPa.

(E) Response and recovery time of the pressure sensor under the pressure of 98 kPa.

(F) Comparison of sensitivity and linear sensing range for different piezoresistive sensors.

(G) Comparison of hysteresis ratio and maximum stress for different piezoresistive sensors.

device under different pressure ranging from 50 kPa to 1.5 MPa. The linear relation of the I-V curves indicates the ohmic contacts were formed between CTS/MXene and copper electrodes. Besides, the slope of the I—V curves increases with the increasing pressure, suggesting the continuous decrease of the pressure sensor's resistivity. All these experimental results indicate the excellent stability and reproducibility of the proposed sensor. Response time is another key parameter of the pressure sensor. The proposed CTS/MXene (EPD) sensor device offers a fast response and relaxation time of 52 ms and 40 ms under the applied pressure of 98 kPa (Figure 2E), enabling the sensor to monitor the physical signals in real time. The response and relaxation time of the sensor under different pressure is provided in Figure S11. As summarized

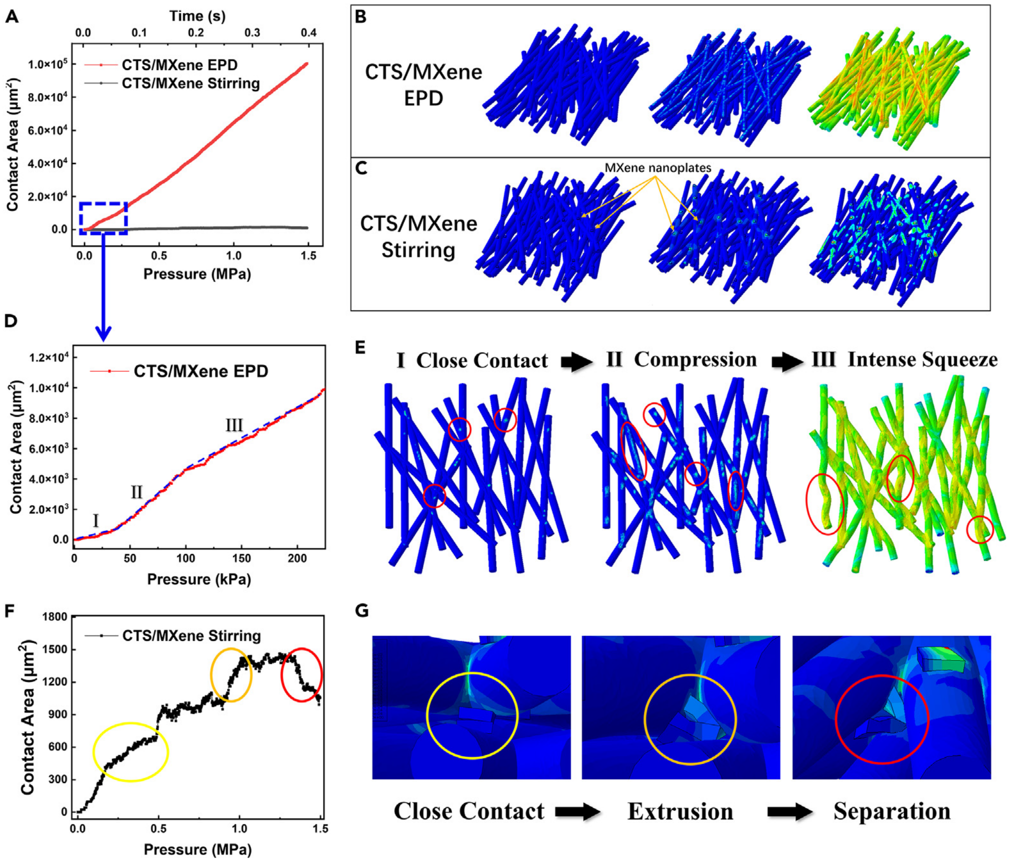

**Figure 3. Finite element analysis of the CTS/MXene pressure sensor**

(A) Contact area as a function of time and pressure for CTS/MXene (EPD) pressure sensor and CTS/MXene (stirring) pressure sensor.

(B and C) Microscopic deformation process for the model with CTS/MXene (EPD) and CTS/MXene (stirring), respectively.

(D) Contact area as a function of pressure for CTS/MXene (EPD) pressure sensor in the range of 0–250 kPa.

(E) Microscopic deformation process for the model with CTS/MXene (EPD), the deformation process can be divided into three stages (close contact-point to point contact, compression-point to point contact and line to line contact, intense squeeze).

(F) Contact area as a function of pressure for CTS/MXene (stirring) pressure sensor in the range of 0–1.5 MPa.

(G) Microscopic deformation process for the model with CTS/MXene (stirring), the deformation process can be divided into three stages (close contact, extrusion, separation).

in Figures 2F and 2G, our CTS/MXene pressure sensor shows greater advantages of high sensitivity within an ultrawide linear range and low hysteresis ratio under incomparably high stress, compared to existing piezoresistive pressure sensors reported in recent literatures.[5,57–72] Furthermore, the complete performance parameters have been benchmarked and compared with other flexible pressure sensors in Table S2.

To better understand the sensing mechanism for CTS/MXene pressure sensor with EPD and stirring process, finite element modeling (FEM) was employed to analyze the dynamic working process of pressure sensors during compression by the software Abaqus. According to the SEM results shown in Figures 1B–1D, we established models for CTS fabrics, MXene nanoplates aggregation, and CTS/MXene (EPD) fabrics. The setup details of simulation are shown in Figures S12–S19. As schematically shown in Figure S6A, agglomerated MXene nanoplates adsorbed onto fibers physically, resulting in few conductivity paths. In contrast, the vast majority of the CTS/MXene fibers (Figure S6C) became conductive in case of 1-h EPD, which benefit from MXene nanoplates adhered to CTS fiber evenly under the action of hydrogen bonding. Therefore, we established conductive models for CTS/MXene (EPD) and CTS/MXene (stirring) in the mode of fibers-to-fibers and nanoplates-to-nanoplates. Figure 3A displays conductive contacting area as a function of time and pressure, collected from the dynamic microscopic deformation processes for two models (Figures 3B and 3C). The relationship between the contact area and conductivity of the sensor is illustrated in Figure S20. The conductivity of CTS/MXene piezoresistive layer is calculated by following formula: $R = \rho L/S$, where R is the total resistance, L is the thickness of the piezoresistive layer, and S is the area of conductive parts. When pressure is applied, the resistance changes from infinite ($+\infty$) to $R_c$, fibers are deformed, resulting in larger contact area (S) and smaller resistance (R), as shown in Figure S20B. Meanwhile, the thickness of the piezoresistive layer (L) is decreasing. As a consequence, the total resistance of CTS/MXene piezoresistive layer decreases, improving the conductivity of the device. For the fibers-to-fibers model, the whole fiber layers stressed uniformly under external pressure, indicating large contact area change and extremely high sensitivity in a linear manner. As the pressure increases from

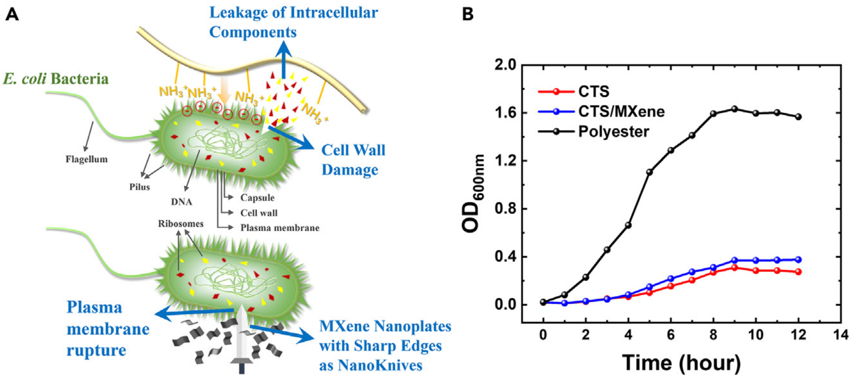

**Figure 4. Antibacterial properties of CTS fabric and CTS/MXene fabric**

(A) The schematic illustration of antibacterial mechanism of CTS and MXene nanoplates.

(B) Antibacterial experiment results of CTS fabrics, CTS/MXene fabrics and polyester fabrics for *E. coli*.

0 to 30 kPa, fiber layers contact with each other in the form of point-to-point, leading to the contact area increment for stage I (Figures 3D and 3E, Video S1). The contact area increases rapidly in the stage II, in which fibers were compressed in the range of 30–100 kPa, ascribing to both the increase of point-to-point contacts and line-to-line contacts. For stage III, fibers will be squeezed when the pressure is greater than 100 kPa. The continuous deformation of fibers, the multiple contacting modes, and high modulus property of CTS/MXene fiber enables the high sensitivity and wide linear range of the pressure sensor. However, for the nanoplates-nanoplates model, the contact mode of nanoplate pairs starts from close contact to extrusion to separation, directly leading to the small contacting area (Figure 3F), uncertain conductive paths or even broken circuits (Figures 3G, Video S2).

Pressure sensors with CTS as the encapsulation layer are more advantageous when applied to wearable devices, because of its merit of antibacterial properties brought by cationic groups on the surfaces of CTS.[43,73,74] Furthermore, MXene was also proven to be antibacterial in previous studies.[75–77] To explore the antibacterial properties of CTS and CTS/MXene, a shake flask method is explored, making full contact between bacteria and the fabric because of the innately antibacterial property of CTS. *E. coli* is cultured in test tubes on a bacterial shaker incubator at 37°C, containing CTS fabrics, CTS/MXene fabrics and polyester fabrics as blank control group, respectively. During 12 h cultivation, the absorbance (OD) of the bacterial solution was measured, as shown in Figure 4B. The $OD_{600}$ stands for the optical density of 600 nm. Obviously, the bacterial solution with polyester shows the highest absorbance intensities of 1.63 for *E. coli* at the ninth hour, considered to be the maximum number of bacteria without any suppression. In comparison, both the CTS fabrics and CTS/MXene fabrics showed a strong inhibitory effect in the first 3 h, ascribing to the destructive effect of cationic groups of CTS on bacteria. As shown in Figure 4A, the interaction between polycationic structure of CTS and the predominantly anionic components of bacteria surface leads to changes in permeability, leakage of intracellular components and death of the cell. Also, owing to the close contact between bacteria and fabrics during violent shaking, sharp edges of MXene nanoplates could rupture the bacterial membrane, which also played a certain inhibitory role. However, the solution absorbance intensity started to grow for CTS fabrics and CTS/MXene fabrics at the fifth hour, which means the antibacterial activity started descending. From the ninth hour, the number of *E. coli* no longer grew any more. The final solution absorbance intensities were 0.27, 0.38, and 1.57, corresponding to CTS fabrics, CTS/MXene fabrics and polyester fabrics, respectively.

For actual wearable applications, we explore the sensor's ability as a skin-mountable human motion detector to real-time monitor biophysical signals. In the test, the fabricated CTS/MXene pressure sensor was attached to various parts of human body, as shown in Figures 5A–5F, including finger joint, arm muscles, palm, wrist joint, neck, and ankle joint. For all the repetitive dynamic flexion and straightening motions of these positions, the CTS/MXene pressure sensor is highly responsive. In cycling test, the response and relaxation behaviors are proved to be reproducible. Deep learning has wide applications in human motion recognition, machine translation and behavior analysis. A multiscale kernel based residual CNN was proposed by Liu et al.[78] Figure S21 depicts the structure and parameters of CNN. Firstly, the multiscale kernel algorithm is applied in the CNN architecture to ensure that different signal intensities are captured. The design of the three-head network is sufficient to ensure that the network can handle different signal intensities. Secondly, in order for the architecture to extract signal features from deep and hierarchical representation spaces, sufficient network depth is required. Therefore, residual learning is embedded into a multiscale kernel CNN to avoid degradation problems and prevent features from being effectively extracted. Based on the previous structural design, the structure of this multi-time scale convolutional network model is very clear, and it can effectively classify input signals. Due to the match with the sequence properties of the sensor signals, we used CNN for sensor-based human motion classification. We tested the prediction ability of the neural network model under different training epochs and different hyperparameters such as learning rate, by monitoring the accuracy in epochs in real time. By training the network model based on our collect 2120 samples, we have achieved a recognition accuracy of 98.61% (Figure 5H). The final model was trained for 20 epochs, and the initial learning rate was 0.001. The accuracy of the third epoch was about 65%, and the accuracy of the seventh epoch reached 90%. The final accuracy was stable at about 98%. We also tested the recall rate, F1 score and other classification model indicators. The

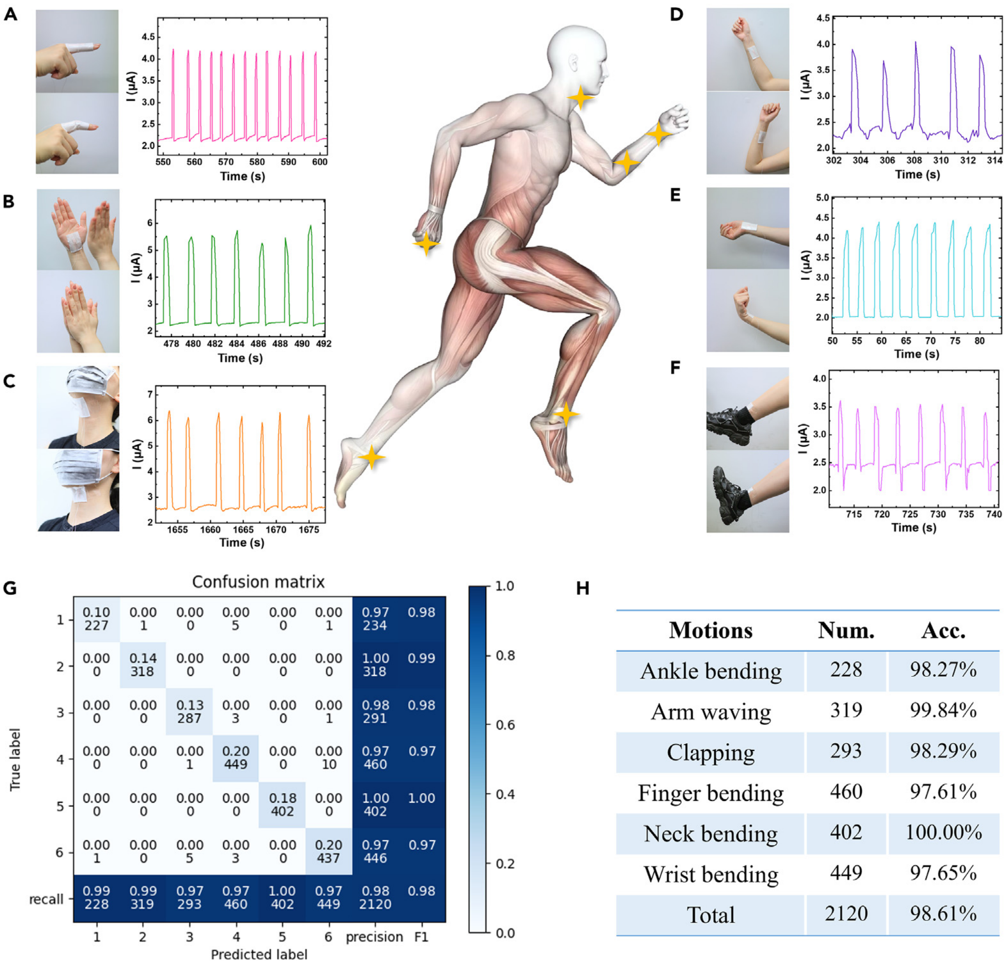

| | 1 | 2 | 3 | 4 | 5 | 6 | precision | F1 |
|---|---|---|---|---|---|---|---|---|
| 1 | 0.10<br>227 | 0.00<br>1 | 0.00<br>0 | 0.00<br>5 | 0.00<br>0 | 0.00<br>1 | 0.97<br>234 | 0.98 |
| 2 | 0.00<br>0 | 0.14<br>318 | 0.00<br>0 | 0.00<br>0 | 0.00<br>0 | 0.00<br>0 | 1.00<br>318 | 0.99 |
| 3 | 0.00<br>0 | 0.00<br>0 | 0.13<br>287 | 0.00<br>3 | 0.00<br>0 | 0.00<br>1 | 0.98<br>291 | 0.98 |
| 4 | 0.00<br>0 | 0.00<br>0 | 0.00<br>1 | 0.20<br>449 | 0.00<br>0 | 0.00<br>10 | 0.97<br>460 | 0.97 |
| 5 | 0.00<br>0 | 0.00<br>0 | 0.00<br>0 | 0.00<br>0 | 0.18<br>402 | 0.00<br>0 | 1.00<br>402 | 1.00 |
| 6 | 0.00<br>1 | 0.00<br>0 | 0.00<br>5 | 0.00<br>3 | 0.00<br>0 | 0.20<br>437 | 0.97<br>446 | 0.97 |
| recall | 0.99<br>228 | 0.99<br>319 | 0.97<br>293 | 0.97<br>460 | 1.00<br>402 | 0.97<br>449 | 0.98<br>2120 | 0.98 |

| Motions | Num. | Acc. |
|---|---|---|
| Ankle bending | 228 | 98.27% |
| Arm waving | 319 | 99.84% |
| Clapping | 293 | 98.29% |
| Finger bending | 460 | 97.61% |
| Neck bending | 402 | 100.00% |
| Wrist bending | 449 | 97.65% |
| Total | 2120 | 98.61% |

**Figure 5. Human action detection and recognition by the CTS/MXene pressure sensor**

(A–F) Human action detection: monitoring finger bending, clapping, neck bending, arm waving, wrist bending, and ankle bending.

(G) The confusion matrix for biophysical action-level classification by CNN.

(H) The statistics of the collected human actions and the accuracy for each one. The total accuracy is 98.61%.

recall rate was 98.5% and the F1 score reached 98.6%. A combination of multiple indicators determined that the model did not have overfitting problems. 5-fold cross-validation was used to train and test our model. In Figure 5G, we show the results tested on the training set, and the ratio of training set to test set is 4:1. In addition, we characterized the sensor's performance by driving a truck over the pressure sensor (~700 kPa) repeatedly, as shown in Figure S22. It is found that the sensor responses quickly and stably under the repeated tests, endowing its good applicability in real-world high pressure scenarios.

## Conclusion

In summary, CTS/MXene fiber composites were constructed by the facile EPD technique and applied in the piezoresistive sensor. Benefiting from the hierarchical yet porous architecture, point-to-line contacting modes, strong chemical interaction, high modulus, as well as excellent mechanical stability of the CTS/MXene fiber, the fabricated pressure sensor displayed outstanding performance including high sensitivity ($1.16\ kPa^{-1}$) within ultrawide linear range (1.5 MPa), a small hysteresis of 5.14% and a low fatigue over 1000 loading/unloading cycles under 1.5 MPa pressure load. The sensor device also possesses good antibacterial effect ascribing from the strong interaction between CTS/MXene and bacteria surface. In addition, the sensor could also be applied in various human action detection. With the help of CNN deep neural network, the sensor could recognize the human action with high accuracy of 98.61%.

## Limitations of the study

We did not investigate decoupled sensing mechanisms of multimodal sensors, as the sensor responds to both pressure and mechanical strain from bending/twisting. The demonstration that directly leverages the antibacterial properties is still needed to be further investigated.

## STAR★METHODS

Detailed methods are provided in the online version of this paper and include the following:

- KEY RESOURCES TABLE
- RESOURCE AVAILABILITY
    - ○ Lead contact
    - ○ Materials availability
    - ○ Data and code availability
- METHOD DETAILS
    - ○ Fabrication of CTS spunlace nonwoven fabrics
    - ○ Preparation of CTS/MXene (EPD), CTS/MXene (stirring) functional layer
    - ○ Encapsulation of CTS/MXene piezoresistive pressure sensor
    - ○ Characterization and test
    - ○ FEA simulation

## SUPPLEMENTAL INFORMATION

Supplemental information can be found online at https://doi.org/10.1016/j.isci.2024.109481.

## ACKNOWLEDGMENTS

This work was partially supported by the Shenzhen Basic Research Grant (JCYJ20200109114801744, JCYJ20220818101402005, and 202211293000152), the National Nature Science Foundation of China (52173243 and 62175252), Guangdong Basic and Applied Basic Research Foundation (2023A1515030113), and Youth Innovation Promotion Association, Chinese Academy of Sciences (2023375). This work was supported in part by the Singapore Ministry of Education Academic Research Fund Tier 2 (MOE2019-T2-2-127), the Singapore Ministry of Education Academic Research Fund Tier 1 (MOE2019-T1-001-103 and MOE2019-T1-001-111), and the Singapore National Research Foundation Competitive Research Program (NRF-CRP18-2017-02). This work was also supported in part by Nanyang Technological University.

## AUTHOR CONTRIBUTIONS

M.G. and X.Z. contributed equally to this work. Conceptualization, M.G., X.Z., and M.C.; methodology, X.Z., J.S., Y.D., and Z.W.; software, M.G. and B.Z.; validation, R.X. and Y.S.; formal analysis, J.L.; investigation, Y.S. and J.G.; writing – original draft, M.G.; writing – review and editing, Lei Wei and M.C.; funding acquisition, C.Y. and M.C.; resources, Y.H., G.G., and Lei Wang; supervision, Lei Wei and M.C.; project administration, Z.W.

## DECLARATION OF INTERESTS

The authors declare no competing interest.

Received: November 15, 2023
Revised: January 15, 2024
Accepted: March 8, 2024
Published: March 11, 2024

## REFERENCES

1. Zhang, Y., Yang, J., Hou, X., Li, G., Wang, L., Bai, N., Cai, M., Zhao, L., Wang, Y., Zhang, J., et al. (2022). Highly stable flexible pressure sensors with a quasi-homogeneous composition and interlinked interfaces. Nat. Commun. *13*, 1317. https://doi.org/10.1038/s41467-022-29093-y.
2. Zhong, M., Zhang, L., Liu, X., Zhou, Y., Zhang, M., Wang, Y., Yang, L., and Wei, D. (2021). Wide linear range and highly sensitive flexible pressure sensor based on multistage sensing process for health monitoring and human-machine interfaces. Chem. Eng. J. *412*, 128649. https://doi.org/10.1016/j.cej.2021.128649.
3. He, F., You, X., Wang, W., Bai, T., Xue, G., and Ye, M. (2021). Recent Progress in Flexible Microstructural Pressure Sensors toward Human–Machine Interaction and Healthcare Applications. Small Methods *5*, 2001041. https://doi.org/10.1002/smtd.202001041.
4. Li, S., Zhang, Y., Wang, Y., Xia, K., Yin, Z., Wang, H., Zhang, M., Liang, X., Lu, H., Zhu, M., et al. (2020). Physical sensors for skin-inspired electronics. InfoMat *2*, 184–211. https://doi.org/10.1002/inf2.12060.
5. Pan, L., Chortos, A., Yu, G., Wang, Y., Isaacson, S., Allen, R., Shi, Y., Dauskardt, R., and Bao, Z. (2014). An ultra-sensitive resistive pressure sensor based on hollow-sphere microstructure induced elasticity in conducting polymer film. Nat. Commun. *5*, 3002. https://doi.org/10.1038/ncomms4002.
6. Yu, Z., Hu, G., Chen, J., Huang, F., Zhao, Y., and Feng, J. (2023). Resonant printing flexible piezoresistive pressure sensor with spherical microstructures. Smart Mater. Struct. *32*, 035020. https://doi.org/10.1088/1361-665X/acb6c9.
7. Kong, H., Song, Z., Li, W., Bao, Y., Qu, D., Ma, Y., Liu, Z., Wang, W., Wang, Z., Han, D., and Niu, L. (2021). Skin-Inspired Hair–Epidermis–Dermis Hierarchical Structures for Electronic Skin Sensors with High Sensitivity over a Wide Linear Range. ACS Nano *15*, 16218–16227. https://doi.org/10.1021/acsnano.1c05199.
8. Song, Z., Li, W., Kong, H., Chen, M., Bao, Y., Wang, N., Wang, W., Liu, Z., Ma, Y., He, Y., et al. (2022). Merkel receptor-inspired integratable and biocompatible pressure sensor with linear and ultrahigh sensitive response for versatile applications. Chem. Eng. J. *444*, 136481. https://doi.org/10.1016/j.cej.2022.136481.
9. Zhi, C., Shi, S., Si, Y., Fei, B., Huang, H., and Hu, J. (2023). Recent Progress of Wearable Piezoelectric Pressure Sensors Based on Nanofibers, Yarns, and Their Fabrics via Electrospinning. Adv. Mater. Technol. *8*, 2201161. https://doi.org/10.1002/admt.202201161.
10. Zeng, X., Wang, Z., Zhang, H., Yang, W., Xiang, L., Zhao, Z., Peng, L.-M., and Hu, Y.

(2019). Tunable, Ultrasensitive, and Flexible Pressure Sensors Based on Wrinkled Microstructures for Electronic Skins. ACS Appl. Mater. Interfaces *11*, 21218–21226. https://doi.org/10.1021/acsami.9b02518.

11. Luo, Y., Shao, J., Chen, S., Chen, X., Tian, H., Li, X., Wang, L., Wang, D., and Lu, B. (2019). Flexible Capacitive Pressure Sensor Enhanced by Tilted Micropillar Arrays. ACS Appl. Mater. Interfaces *11*, 17796–17803. https://doi.org/10.1021/acsami.9b03718.
12. Liu, S., Song, Z., Chen, M., Li, W., Ma, Y., Liu, Z., Bao, Y., Mahmood, A., and Niu, L. (2023). Modulus difference-induced embedding strategy to construct iontronic pressure sensor with high sensitivity and wide linear response range. iScience *26*, 107304. https://doi.org/10.1016/j.isci.2023.107304.
13. Lee, Y., Park, J., Cho, S., Shin, Y.-E., Lee, H., Kim, J., Myoung, J., Cho, S., Kang, S., Baig, C., and Ko, H. (2018). Flexible Ferroelectric Sensors with Ultrahigh Pressure Sensitivity and Linear Response over Exceptionally Broad Pressure Range. ACS Nano *12*, 4045–4054. https://doi.org/10.1021/acsnano.8b01805.
14. Zhong, Y., Wang, J., Han, L., Dai, S., Zhu, H., Hua, J., Cheng, G., and Ding, J. (2023). High-performance flexible self-powered triboelectric pressure sensor based on chemically modified micropatterned PDMS film. Sensor Actuator Phys. *349*, 114013. https://doi.org/10.1016/j.sna.2022.114013.
15. Cui, X., Jiang, Y., Hu, L., Cao, M., Xie, H., Zhang, X., Huang, F., Xu, Z., and Zhu, Y. (2023). Synergistically Microstructured Flexible Pressure Sensors with High Sensitivity and Ultrawide Linear Range for Full-Range Human Physiological Monitoring. Adv. Mater. Technol. *8*, 2200609. https://doi.org/10.1002/admt.202200609.
16. Luo, R., Cui, Y., Li, H., Wu, Y., Du, B., Zhou, S., and Hu, J. (2023). Fragmented Graphene Aerogel/Polydimethylsiloxane Sponges for Wearable Piezoresistive Pressure Sensors. ACS Appl. Nano Mater. *6*, 7065–7076. https://doi.org/10.1021/acsanm.3c01285.
17. Wu, L., Zhang, Q., and Ming, J. (2023). Facile fabrication of multifunctional polyurethane composite sponge toward strain/pressure sensors and highly efficient oil-water separation. Ind. Crop. Prod. *193*, 116179. https://doi.org/10.1016/j.indcrop.2022.116179.
18. Wang, G., Wang, M., Zheng, M., Ebo, B., Xu, C., Liu, Z., and He, L. (2023). Thermoplastic Polyurethane/Carbon Nanotube Composites for Stretchable Flexible Pressure Sensors. ACS Appl. Nano Mater. *6*, 9865–9873. https://doi.org/10.1021/acsanm.3c01543.
19. Yang, W., Liu, H., Du, H., Zhang, M., Wang, C., Yin, R., Pan, C., Liu, C., and Shen, C. (2023). Robust and superelastic spider web-like polyimide fiber-based conductive composite aerogel for extreme temperature-tolerant linear pressure sensor. Sci. China Mater. *66*, 2829–2842. https://doi.org/10.1007/s40843-022-2418-1.
20. Jia, M., Yi, C., Han, Y., Wang, L., Li, X., Xu, G., He, K., Li, N., Hou, Y., Wang, Z., et al. (2022). Hierarchical Network Enabled Flexible Textile Pressure Sensor with Ultrabroad Response Range and High-Temperature Resistance. Adv. Sci. *9*, 2105738. https://doi.org/10.1002/advs.202105738.
21. Hasenkamp, W., Forchelet, D., Pataky, K., Villard, J., Van Lintel, H., Bertsch, A., Wang, Q., and Renaud, P. (2012). Polyimide/SU-8 catheter-tip MEMS gauge pressure sensor. Biomed. Microdevices *14*, 819–828. https://doi.org/10.1007/s10544-012-9661-8.
22. Qin, R., Li, X., Hu, M., Shan, G., Seeram, R., and Yin, M. (2022). Preparation of high-performance MXene/PVA-based flexible pressure sensors with adjustable sensitivity and sensing range. Sensor Actuator Phys. *338*, 113458. https://doi.org/10.1016/j.sna.2022.113458.
23. Hou, Y., Wang, L., Sun, R., Zhang, Y., Gu, M., Zhu, Y., Tong, Y., Liu, X., Wang, Z., Xia, J., et al. (2022). Crack-Across-Pore Enabled High-Performance Flexible Pressure Sensors for Deep Neural Network Enhanced Sensing and Human Action Recognition. ACS Nano *16*, 8358–8369. https://doi.org/10.1021/acsnano.2c02609.
24. Zhao, L., Qiang, F., Dai, S.-W., Shen, S.-C., Huang, Y.-Z., Huang, N.-J., Zhang, G.-D., Guan, L.-Z., Gao, J.-F., Song, Y.-H., and Tang, L.C. (2019). Construction of sandwich-like porous structure of graphene-coated foam composites for ultrasensitive and flexible pressure sensors. Nanoscale *11*, 10229–10238. https://doi.org/10.1039/C9NR02672J.
25. Choi, D., Kim, D.W., Yoo, D., Cha, K.J., La, M., and Kim, D.S. (2017). Spontaneous occurrence of liquid-solid contact electrification in nature: Toward a robust triboelectric nanogenerator inspired by the natural lotus leaf. Nano Energy *36*, 250–259. https://doi.org/10.1016/j.nanoen.2017.04.026.
26. Liu, L.-X., Chen, W., Zhang, H.-B., Wang, Q.-W., Guan, F., and Yu, Z.-Z. (2019). Flexible and Multifunctional Silk Textiles with Biomimetic Leaf-Like MXene/Silver Nanowire Nanostructures for Electromagnetic Interference Shielding, Humidity Monitoring, and Self-Derived Hydrophobicity. Adv. Funct. Mater. *29*, 1905197. https://doi.org/10.1002/adfm.201905197.
27. Zhang, X., Chen, F., Han, L., Zhang, G., Hu, Y., Jiang, W., Zhu, P., Sun, R., and Wong, C.-P. (2021). Flexible, Highly Sensitive, and Ultrafast Responsive Pressure Sensor with Stochastic Microstructures for Human Health Monitoring. Adv. Eng. Mater. *23*, 2000902. https://doi.org/10.1002/adem.202000902.
28. Sun, F., Liu, L., Liu, T., Wang, X., Qi, Q., Hang, Z., Chen, K., Xu, J., and Fu, J. (2023). Vascular smooth muscle-inspired architecture enables soft yet tough self-healing materials for durable capacitive strain-sensor. Nat. Commun. *14*, 130. https://doi.org/10.1038/s41467-023-35810-y.
29. Zhao, T., Li, T., Chen, L., Yuan, L., Li, X., and Zhang, J. (2019). Highly Sensitive Flexible Piezoresistive Pressure Sensor Developed Using Biomimetically Textured Porous Materials. ACS Appl. Mater. Interfaces *11*, 29466–29473. https://doi.org/10.1021/acsami.9b09265.
30. Chen, M., Li, K., Cheng, G., He, K., Li, W., Zhang, D., Li, W., Feng, Y., Wei, L., Li, W., et al. (2019). Touchpoint-Tailored Ultrasensitive Piezoresistive Pressure Sensors with a Broad Dynamic Response Range and Low Detection Limit. ACS Appl. Mater. Interfaces *11*, 2551–2558. https://doi.org/10.1021/acsami.8b20284.
31. Li, W., Xiong, L., Li, N., Pang, S., Xu, G., Yi, C., Wang, Z., Gu, G., Li, K., Li, W., et al. (2019). Tunable 3D light trapping architectures based on self-assembled $SnSe_2$ nanoplate arrays for ultrasensitive SERS detection. J. Mater. Chem. C *7*, 10179–10186. https://doi.org/10.1039/C9TC03715B.
32. Wang, S., Deng, W., Yang, T., Ao, Y., Zhang, H., Tian, G., Deng, L., Huang, H., Huang, J., Lan, B., and Yang, W. (2023). Bioinspired MXene-Based Piezoresistive Sensor with Two-stage Enhancement for Motion Capture. Adv. Funct. Mater. *33*, 2214503. https://doi.org/10.1002/adfm.202214503.
33. Yang, R., Dutta, A., Li, B., Tiwari, N., Zhang, W., Niu, Z., Gao, Y., Erdely, D., Xin, X., Li, T., and Cheng, H. (2023). Iontronic pressure sensor with high sensitivity over ultra-broad linear range enabled by laser-induced gradient micro-pyramids. Nat. Commun. *14*, 2907. https://doi.org/10.1038/s41467-023-38274-2.
34. Yang, R., Zhang, W., Tiwari, N., Yan, H., Li, T., and Cheng, H. (2022). Multimodal Sensors with Decoupled Sensing Mechanisms. Adv. Sci. *9*, 2202470. https://doi.org/10.1002/advs.202202470.
35. Lai, Y.-C., Ye, B.-W., Lu, C.-F., Chen, C.-T., Jao, M.-H., Su, W.-F., Hung, W.-Y., Lin, T.-Y., and Chen, Y.-F. (2016). Extraordinarily Sensitive and Low-Voltage Operational Cloth-Based Electronic Skin for Wearable Sensing and Multifunctional Integration Uses: A Tactile-Induced Insulating-to-Conducting Transition. Adv. Funct. Mater. *26*, 1286–1295. https://doi.org/10.1002/adfm.201503606.
36. Zhang, S., Zhu, J., Zhang, Y., Chen, Z., Song, C., Li, J., Yi, N., Qiu, D., Guo, K., Zhang, C., et al. (2022). Standalone stretchable RF systems based on asymmetric 3D microstrip antennas with on-body wireless communication and energy harvesting. Nano Energy *96*, 107069. https://doi.org/10.1016/j.nanoen.2022.107069.
37. Xue, Y., Wang, Z., Dutta, A., Chen, X., Gao, P., Li, R., Yan, J., Niu, G., Wang, Y., Du, S., et al. (2023). Superhydrophobic, stretchable kirigami pencil-on-paper multifunctional device platform. Chem. Eng. J. *465*, 142774. https://doi.org/10.1016/j.cej.2023.142774.
38. Zhang, C., Chen, J., Gao, J., Tan, G., Bai, S., Weng, K., Chen, H.M., Ding, X., Cheng, H., Yang, Y., and Wang, J. (2023). Laser Processing of Crumpled Porous Graphene/MXene Nanocomposites for a Standalone Gas Sensing System. Nano Lett. *23*, 3435–3443. https://doi.org/10.1021/acs.nanolett.3c00454.
39. Sun, Y., Tai, H., Yuan, Z., Duan, Z., Huang, Q., and Jiang, Y. (2021). A Facile Strategy for Low Young's Modulus PDMS Microbeads Enhanced Flexible Capacitive Pressure Sensors. Part. Part. Syst. Charact. *38*, 2100019. https://doi.org/10.1002/ppsc.202100019.
40. Zhu, Y., Wu, Y., Wang, G., Wang, Z., Tan, Q., Zhao, L., and Wu, D. (2020). A flexible capacitive pressure sensor based on an electrospun polyimide nanofiber membrane. Org. Electron. *84*, 105759. https://doi.org/10.1016/j.orgel.2020.105759.
41. Rinaudo, M., Auzely, R., Vallin, C., and Mullagaliev, I. (2005). Specific Interactions in Modified Chitosan Systems. Biomacromolecules *6*, 2396–2407. https://doi.org/10.1021/bm0580025.
42. Toskas, G., Brünler, R., Hund, H., Hund, R.-D., Hild, M., Aibibu, D., and Cherif, C. (2013). Pure chitosan microfibres for biomedical applications. Autex Res. J. *13*, 134–140. https://doi.org/10.2478/v10304-012-0041-5.
43. Saini, S., Gupta, A., Singh, N., and Sheikh, J. (2020). Functionalization of linen fabric using layer by layer treatment with chitosan and green tea extract. J. Ind. Eng. Chem. *82*, 138–143. https://doi.org/10.1016/j.jiec.2019.10.005.
44. Abu El-Soad, A.M., Lazzara, G., Abd El-Magied, M.O., Cavallaro, G., Al-Otaibi, J.S., Sayyed, M.I., and Kovaleva, E.G. (2022). Chitosan Functionalized with Carboxyl Groups as a Recyclable Biomaterial for the Adsorption of Cu (II) and Zn (II) Ions in

Aqueous Media. Int. J. Mol. Sci. *23*, 2396. https://doi.org/10.3390/ijms23042396.

45. Dhiman, G., and Chakraborty, J.N. (2015). Antimicrobial performance of cotton finished with triclosan, silver and chitosan. Fashion Textiles *2*, 13. https://doi.org/10.1186/s40691-015-0040-y.
46. Xie, X., Zhao, M.-Q., Anasori, B., Maleski, K., Ren, C.E., Li, J., Byles, B.W., Pomerantseva, E., Wang, G., and Gogotsi, Y. (2016). Porous heterostructured MXene/carbon nanotube composite paper with high volumetric capacity for sodium-based energy storage devices. Nano Energy *26*, 513–523. https://doi.org/10.1016/j.nanoen.2016.06.005.
47. Gogotsi, Y., and Anasori, B. (2019). The Rise of MXenes. ACS Nano *13*, 8491–8494. https://doi.org/10.1021/acsnano.9b06394.
48. Wang, Q., Pan, X., Lin, C., Gao, H., Cao, S., Ni, Y., and Ma, X. (2020). Modified Ti3C2TX (MXene) nanosheet-catalyzed self-assembled, anti-aggregated, ultra-stretchable, conductive hydrogels for wearable bioelectronics. Chem. Eng. J. *401*, 126129. https://doi.org/10.1016/j.cej.2020.126129.
49. Ding, Y., Liu, Y., Sun, X., Yao, Y., Yuan, B., Huang, T., and Tang, J. (2022). Three-dimensional ordered and porous Ti3C2Tx@Chitosan film enabled by self-assembly strategy for high-rate pseudocapacitive energy storage. Chem. Eng. J. *442*, 136255. https://doi.org/10.1016/j.cej.2022.136255.
50. Zhan, J., Sun, H., Xie, M., Han, J., Chen, L., and Zhao, Y. (2022). Hyperbranched polyamidoamine-chitosan polyelectrolyte gels crosslinking by polyacrylic acid and alginate for removal of anionic dyes. Int. J. Biol. Macromol. *222*, 3024–3033. https://doi.org/10.1016/j.ijbiomac.2022.10.077.
51. Yousaf, T., Areeb, A., Murtaza, M., Munir, A., Khan, Y., and Waseem, A. (2022). Silane-Grafted MXene (Ti3C2TX) Membranes for Enhanced Water Purification Performance. ACS Omega *7*, 19502–19512. https://doi.org/10.1021/acsomega.2c01143.
52. Kiran, N.U., Deore, A.B., More, M.A., Late, D.J., Rout, C.S., Mane, P., Chakraborty, B., Besra, L., and Chatterjee, S. (2022). Comparative Study of Cold Electron Emission from 2D Ti3C2TX MXene Nanosheets with Respect to Its Precursor Ti3SiC2 MAX Phase. ACS Appl. Electron. Mater. *4*, 2656–2666. https://doi.org/10.1021/acsaelm.2c00128.
53. Krishna, Y., Saidur, R., Aslfattahi, N., Faizal, M., and Ng, K.C. (2020). Enhancing the thermal properties of organic phase change material (palmitic acid) by doping MXene nanoflakes. AIP Conf. Proc. *2233*, 020013. https://doi.org/10.1063/5.0001366.
54. Xiu, L., Pei, W., Zhou, S., Wang, Z., Yang, P., Zhao, J., and Qiu, J. (2020). Multilevel Hollow MXene Tailored Low-Pt Catalyst for Efficient Hydrogen Evolution in Full-pH Range and Seawater. Adv. Funct. Mater. *30*, 1910028. https://doi.org/10.1002/adfm.201910028.
55. Zhao, M.-Q., Ren, C.E., Ling, Z., Lukatskaya, M.R., Zhang, C., Van Aken, K.L., Barsoum, M.W., and Gogotsi, Y. (2015). Flexible MXene/Carbon Nanotube Composite Paper with High Volumetric Capacitance. Adv. Mater. *27*, 339–345. https://doi.org/10.1002/adma.201404140.
56. Lamiel, C., Hussain, I., Ogunsakin, O.R., and Zhang, K. (2022). MXene in core–shell structures: research progress and future prospects. J. Mater. Chem. A Mater. *10*, 14247–14272. https://doi.org/10.1039/D2TA02255A.
57. Shi, J., Wang, L., Dai, Z., Zhao, L., Du, M., Li, H., and Fang, Y. (2018). Multiscale Hierarchical Design of a Flexible Piezoresistive Pressure Sensor with High Sensitivity and Wide Linearity Range. Small *14*, 1800819. https://doi.org/10.1002/smll.201800819.
58. Chen, B., Zhang, L., Li, H., Lai, X., and Zeng, X. (2022). Skin-inspired flexible and high-performance MXene@polydimethylsiloxane piezoresistive pressure sensor for human motion detection. J. Colloid Interface Sci. *617*, 478–488. https://doi.org/10.1016/j.jcis.2022.03.013.
59. Zhu, G., Dai, H., Yao, Y., Tang, W., Shi, J., Yang, J., and Zhu, L. (2022). 3D Printed Skin-Inspired Flexible Pressure Sensor with Gradient Porous Structure for Tunable High Sensitivity and Wide Linearity Range. Adv. Mater. Technol. *7*, 2101239. https://doi.org/10.1002/admt.202101239.
60. Shi, Y., Lü, X., Wang, W., Meng, X., Zhao, J., Wang, P., and Bai, G. (2021). Multilayer Flexible Pressure Sensor With High Sensitivity Over Wide Linearity Detection Range (August 2021). IEEE Trans. Instrum. Meas. *70*, 1–9. https://doi.org/10.1109/TIM.2021.3101307.
61. Guan, H., Meng, J., Cheng, Z., and Wang, X. (2020). Processing Natural Wood into a High-Performance Flexible Pressure Sensor. ACS Appl. Mater. Interfaces *12*, 46357–46365. https://doi.org/10.1021/acsami.0c12561.
62. Xu, J., Li, H., Yin, Y., Li, X., Cao, J., Feng, H., Bao, W., Tan, H., Xiao, F., and Zhu, G. (2022). High sensitivity and broad linearity range pressure sensor based on hierarchical in-situ filling porous structure. npj Flex. Electron. *6*, 62. https://doi.org/10.1038/s41528-022-00191-7.
63. Xu, Z., Wu, D., Chen, Z., Wang, Z., Cao, C., Shao, X., Zhou, G., Zhang, S., Wang, L., and Sun, D. (2023). A flexible pressure sensor with highly customizable sensitivity and linearity via positive design of microhierarchical structures with a hyperelastic model. Microsyst. Nanoeng. *9*, 5–12. https://doi.org/10.1038/s41378-022-00477-w.
64. Tang, Z., Jia, S., Zhou, C., and Li, B. (2020). 3D Printing of Highly Sensitive and Large-Measurement-Range Flexible Pressure Sensors with a Positive Piezoresistive Effect. ACS Appl. Mater. Interfaces *12*, 28669–28680. https://doi.org/10.1021/acsami.0c06977.
65. Chang, S.R., Yang, C.F., Chen, K.H., Liu, H., and Cheng, B. (2019). A high-sensitivity and low-hysteresis flexible pressure sensor based on carbonized cotton fabric. Maturitas *126*, 45–50. https://doi.org/10.1016/j.sna.2019.05.011.
66. Chen, J., Zhang, J., Hu, J., Luo, N., Sun, F., Venkatesan, H., Zhao, N., and Zhang, Y. (2022). Ultrafast-Response/Recovery Flexible Piezoresistive Sensors with DNA-Like Double Helix Yarns for Epidermal Pulse Monitoring. Adv. Mater. *34*, 2104313. https://doi.org/10.1002/adma.202104313.
67. Liang, C., Sun, J., Liu, Z., Tian, G., Liu, Y., Zhao, Q., Yang, D., Chen, J., Zhong, B., Zhu, M., et al. (2023). Wide Range Strain Distributions on the Electrode for Highly Sensitive Flexible Tactile Sensor with Low Hysteresis. ACS Appl. Mater. Interfaces *15*, 15096–15107. https://doi.org/10.1021/acsami.2c21241.
68. Zhou, Q., Chen, T., Cao, S., Xia, X., Bi, Y., and Xiao, X. (2021). A novel flexible piezoresistive pressure sensor based on PVDF/PVA-CNTs electrospun composite film. Appl. Phys. A *127*, 667. https://doi.org/10.1007/s00339-021-04797-y.
69. Oh, J., Kim, D.-Y., Kim, H., Hur, O.-N., and Park, S.-H. (2022). Comparative Study of Carbon Nanotube Composites as Capacitive and Piezoresistive Pressure Sensors under Varying Conditions. Materials *15*, 7637. https://doi.org/10.3390/ma15217637.
70. Cheng, W., Yu, L., Kong, D., Yu, Z., Wang, H., Ma, Z., Wang, Y., Wang, J., Pan, L., and Shi, Y. (2018). Fast-Response and Low-Hysteresis Flexible Pressure Sensor Based on Silicon Nanowires. IEEE Electron. Device Lett. *39*, 1069–1072. https://doi.org/10.1109/LED.2018.2835467.
71. Yao, H., Yang, W., Cheng, W., Tan, Y.J., See, H.H., Li, S., Ali, H.P.A., Lim, B.Z.H., Liu, Z., and Tee, B.C.K. (2020). Near–hysteresis-free soft tactile electronic skins for wearables and reliable machine learning. Proc. Natl. Acad. Sci. USA *117*, 25352–25359. https://doi.org/10.1073/pnas.2010989117.
72. Oh, J., Kim, J.-O., Kim, Y., Choi, H.B., Yang, J.C., Lee, S., Pyatykh, M., Kim, J., Sim, J.Y., and Park, S. (2019). Highly Uniform and Low Hysteresis Piezoresistive Pressure Sensors Based on Chemical Grafting of Polypyrrole on Elastomer Template with Uniform Pore Size. Small *15*, 1901744. https://doi.org/10.1002/smll.201901744.
73. Mocanu, G., Nichifor, M., Mihai, D., and Oproiu, L.C. (2013). Bioactive cotton fabrics containing chitosan and biologically active substances extracted from plants. Mater. Sci. Eng. C Mater. Biol. Appl. *33*, 72–77. https://doi.org/10.1016/j.msec.2012.08.007.
74. Jiang, Z., Li, L., Li, H., Xia, L., Hu, H., Wang, S., Liu, C., Chi, J., Yang, Y., Song, F., et al. (2022). Preparation, biocompatibility, and wound healing effects of O-carboxymethyl chitosan nonwoven fabrics in partial-thickness burn model. Carbohydr. Polym. *280*, 119032. https://doi.org/10.1016/j.carbpol.2021.119032.
75. Rasool, K., Helal, M., Ali, A., Ren, C.E., Gogotsi, Y., and Mahmoud, K.A. (2016). Antibacterial Activity of Ti3C2Tx MXene. ACS Nano *10*, 3674–3684. https://doi.org/10.1021/acsnano.6b00181.
76. Seidi, F., Arabi Shamsabadi, A., Dadashi Firouzjaei, M., Elliott, M., Saeb, M.R., Huang, Y., Li, C., Xiao, H., and Anasori, B. (2023). MXenes Antibacterial Properties and Applications: A Review and Perspective. Small *19*, 2206716. https://doi.org/10.1002/smll.202206716.
77. Rajavel, K., Shen, S., Ke, T., and Lin, D. (2019). Achieving high bactericidal and antibiofouling activities of 2D titanium carbide (Ti3C2Tx) by delamination and intercalation. 2D Mater. *6*, 035040. https://doi.org/10.1088/2053-1583/ab23ce.
78. Liu, R., Wang, F., Yang, B., and Qin, S.J. (2020). Multiscale Kernel Based Residual Convolutional Neural Network for Motor Fault Diagnosis Under Nonstationary Conditions. IEEE Trans. Industr. Inform. *16*, 3797–3806. https://doi.org/10.1109/TII.2019.2941868.

## STAR★METHODS

### KEY RESOURCES TABLE

| REAGENT or RESOURCE | SOURCE | IDENTIFIER |
|---|---|---|
| Bacterial and virus strains | | |
| Escherichia coli | BNCC | BNCC336902 |
| Chemicals, peptides, and recombinant proteins | | |
| Chitosan | Shanghai Aladdin Biochemical Technology Co., Ltd. | CAS: 9012-76-4 |
| MXene | Foshan Xinxi Technology Co. Ltd. | N/A |
| Software and algorithms | | |
| Abaqus 2022 | Dassault Systèmes | https://www.3ds.com/products/simulia/abaqus |

## RESOURCE AVAILABILITY

### Lead contact

Further information and requests for resources and reagents should be directed to and will be fulfilled by the Lead Contact, Ming Chen (ming.chen2@siat.ac.cn).

### Materials availability

This study did not generate new unique reagents.

### Data and code availability

All data reported in this paper will be shared by the lead contact upon request.

This paper does not report original code.

Any additional information required to reanalyze the data reported in this paper is available from the lead contact upon reasonable request.

## METHOD DETAILS

### Fabrication of CTS spunlace nonwoven fabrics

First, 100 g CTS with a DA of 95% is dissolved in 1.26 L of aqueous acetic acid solution to obtain CTS solution with concentration of 8.0%–8.5% wt. Then, the CTS solution is transferred to the wet spinning machine container and stirred for 12 h. After stirring, the solution is heated up to 60°C and immediately ejected through a jet nozzle with 20 μm diameter holes into the coagulation bath which composed of 0.5 M NaOH/10% EtOH and heated up to 30°C. The as-spun fibers are washed in a 30°C water bath and in three 20°C water baths. Afterward, the CTS fibers pass the air-drying units four times and are wound up to bobbins at a take-up speed up to 25 m/min. Finally, arrange the fibers in the water tank according to a certain orientation and bond them at 30 bars water pressure on both sides of the fabrics to get CTS spunlace nonwoven fabrics.

### Preparation of CTS/MXene (EPD), CTS/MXene (stirring) functional layer

MXene was purchased from Foshan Xinxi Technology Co. Ltd., which is LiF/HCl-etched. CTS/MXene (EPD): Firstly, 0.2 g MXene was dispersed in 200 mL of deionized water and sonicated for 20 min to obtain MXene/deionized water electrolyte solution. Secondly, 10 mm (length) × 10 mm (width) CTS fabric was prepared, sticking on the surface of a piece of stainless steel. The piece of stainless steel with CTS fabric was placed in the MXene/deionized water electrolyte solution as the anode, and another piece of stainless steel was placed at a fixed distance from the anode as the cathode. The electrophoretic deposition (EPD) process lasted for 0.5 h, 1 h and 1.5 h under a direct current of 5 V, especially (Figure S23). Finally, the prepared CTS/MXene (EPD) fabric was dried at 60°C for 30 min to obtain CTS/MXene (EPD) functional layer. CTS/MXene (stirring): CTS fabric of the same size was immersed in the above MXene/deionized water electrolyte solution and stirred using a magnetic stirrer for 1 h. The CTS/MXene (stirring) fabric was then dried at 60°C for 30 min to obtain CTS/MXene (stirring) functional layer.

### Encapsulation of CTS/MXene piezoresistive pressure sensor

A pair of copper foils with suitable shape were placed on both sides of the functional layer. CTS fabrics as encapsulation were cut into two pieces of suitable size according to the needs, placed on both sides of the copper foils. Two layers of CTS fabrics were strong bonded with a hot melt adhesive lining in the middle.

### Characterization and test

The microtopography of the CTS and CTS/MXene functional layer was characterized by VEGA3 TESCAN. For FTIR measurement, Frontier was used. The compression test used a JISC MAX-1kN-P-2 automatic load tester. An intelligent testing and data-acquisition platform was designed (Figure S24). The pressure test was given by a pressure meter from Dongguan Zhiqu Precision Instrument Co, Ltd., and all the current data caused by changing pressure processes were collected by a semiconductor parameter analyzer Keithley 2400 series. An oscilloscope (LUCK-3, digital storage oscilloscope, Chengdu Rongte Instrument Co., Ltd.) was used to measure the response time and the recovery time. For the detection limit test, we first put a polished glass slide (~456 Pa) on the fabricated pressure sensor, and then put a piece of PEEK film on the glass slide. With the glass slide, the initial current is 8.5 μA. There are two purposes of this method: (1) make the response current more stable, (2) make the applied pressure more even in consideration of the uneven contact surfaces of the curved PEEK film. With regard to the test on the pressure sensors' response and recovery time, we released a 2 kg weight, a 1 kg weight and a 5 g glass piece on the pressure sensor, respectively. The oscilloscope (LUCK-3, digital storage oscilloscope, Chengdu Rongte Instrument Co., Ltd.) was used for collecting the response voltage data.

### FEA simulation

In order to theoretically study the working mechanism and sensing performance of the pressure sensor, Abaqus 2022 software was adopted in the simulation. Both the model building and further analysis was conducted with Abaqus 2022 software. The CTS fabric was modeled as a homogeneous isotropic elastic material with Young's modulus $E = 2.06$ GPa, and Poisson's ratio $v = 0.4$.